# Integration of Three-Phase *LLC* Resonant Converter and Full-Bridge Converter for Hybrid Modulated Multioutput Topology

Guangdi Li, *Member, IEEE*, Dongsheng Yang, *Senior Member, IEEE*, Bowen Zhou, *Member, IEEE*, Yan-Fei Liu, *Fellow, IEEE*, and Huaguang Zhang, *Fellow, IEEE*

***Abstract*— A multioutput dc–dc topology based on hybrid modulation of pulse frequency modulation and the phase shift is proposed in this article. The proposed hybrid modulated multioutput converter is derived from the integration of a three-phase *LLC* resonant converter and the full-bridge converter. With the hybrid modulation, the multioutput is controlled independently free from cross-regulation and isolated from each other. With the three-phase interleaving operation, the resonant currents can be reduced, and thus, the efficiency will be improved. Furthermore, the output current ripple of the main output voltage is reduced; as a consequence, the lifetime of the output filter capacitor is extended, and the reliability is reinforced. What is more, the number of the power switches is reduced, and the zero-voltage switching of the power switches can be achieved within the entire load range by the proposed integrated topology. All the abovementioned features of the proposed converter will lead to a compact, efficient, and cost-effective design. Finally, a 1.4-kW triple-output laboratory prototype is built and tested to validate the feasibility and effectiveness of the proposed converter.**

***Index Terms*— Full-bridge converter, hybrid modulation, multioutput dc–dc converter, three-phase *LLC* resonant converter.**

## I. Introduction

MULTIOUTPUT dc–dc converters are found widely used in various applications, such as telecommunication power supplies, consumer electronics, renewable energy systems, battery chargers, and EVs [1]–[5]. The multioutput converters are a kind of converters whose output voltages are derived from the single-input converter, which shows higher power density and lower system cost with reduced power switches compared to the several single-output dc–dc converters solutions. The commonly multioutput dc–dc converters are derived from the classical dc–dc converters, such as buck, boost, and cuk.

Yang *et al.* [6], Shafiei *et al.* [7], and Lee *et al.* [8] introduce some commonly used high-frequency isolated dc–dc converters; among the various dc–dc converters with high-frequency isolation, full-bridge converter and *LLC* resonant converter are two types of converters that attract great interests of research for their soft-switching performance, high efficiency, and high power density. The full-bridge converter [9], [10], whose output voltage is controlled by the phase angle between the bridge branches, can achieve zero-voltage switching (ZVS) without an additional auxiliary circuit; as a result, the main features of the full-bridge converter include high efficiency and high power density. However, the full-bridge converter has several drawbacks, including the following: the ZVS operation will lose under light load conditions, which leads to decreased efficiency and high electromagnetic interference (EMI) [11]; the diodes of the secondary side operate in hard switching, and the parasitic oscillation across the rectifier increases the voltage stress of devices and causes output noise [9]; and a large series inductance will be needed to achieve the ZVS operation, which will cause duty cycle loss and high voltage spikes on the secondary side rectifiers [12]. Some countermeasures have been proposed to mitigate the aforementioned constraints [13], [14]. However, these countermeasures need extra clamp circuits, which will decrease the power density.

The resonant converters [15], [16], whose output voltage is regulated by the switching frequency. Compared to the full-bridge converters, the resonant converters can achieve soft-switching operation within the entire load range by the resonance of the resonant capacitor and the resonant inductor. The *LLC* resonant converters are widely used as the dc–dc stage due to their superior performance [17]–[19]. Nevertheless, the resonant converters have also some drawbacks, including the following: the resonant current is usually large, which will increase the conduction loss and decrease the efficiency [20]; the large output current ripple is also large, which will shorten the lifetime of the output capacitor and degrade the reliability of the power converters [21]. In order

Manuscript received 2 June 2021; revised 1 September 2021 and 9 November 2021; accepted 22 December 2021. Date of publication 31 December 2021; date of current version 3 October 2022. This work was supported in part by the State Key Laboratory of Alternate Electrical Power System with Renewable Energy Sources under Grant LAPS21007, in part by the Guangdong Basic and Applied Basic Research Foundation, in part by the Fundamental Research Funds for the Central Universities under Grant N2104014 and Grant N180415004, in part by the National Key Research and Development Program of China under Grant 2018YFB1700500, in part by the National Natural Science Foundation of China under Grant U1908217, and in part by the Liaoning Revitalization Talents Program under Grant XLYC1902055. Recommended for publication by Associate Editor Santanu Kapat. *(Corresponding author: Dongsheng Yang.)*

Guangdi Li, Dongsheng Yang, Bowen Zhou, and Huaguang Zhang are with the College of Information Science and Engineering, Northeastern University, Shenyang, China (e-mail: liguangdi@mail.neu.edu.cn; yangdongsheng@mail.neu.edu.cn; zhoubowen@mail.neu.edu.cn; hgzhang@ieee.org).

Yan-Fei Liu is with the Department of Electrical and Computer Engineering, Queen's University, Kingston, ON K7L 3N6, Canada (e-mail: yanfei.liu@queesu.ca).

Color versions of one or more figures in this article are available at https://doi.org/10.1109/JESTPE.2021.3139905.

Digital Object Identifier 10.1109/JESTPE.2021.3139905

to decrease the resonant current, the multiphase resonant converters have been presented [22]–[25]. Due to the multiphase architecture, the converters have advantages of lower resonant current and reduced output current ripple allowing small-size filter requirements. Among the various multiphase dc–dc converters, the three-phase architecture is one of the most popular multiphase architectures that have been studied in [26]–[28]. It has been proven in [29] that the three-phase interleaved *LLC* resonant converter can achieve automatic current sharing by interconnecting the primary sides into a common Y node [30] and the secondary sides into a common Y-node [24]. Furthermore, the three inductors and transformers can be integrated into one magnetic component [29], which can increase the power density.

A variety of multioutput converters have been reported in recent literature. Prieto *et al.* [31] present a multioutput topology derived methodology for single-input–multi-output applications based on single-switched nonisolated dc–dc converters. With the presented topological construction method, one can obtain a variety of multioutput converters based on the buck, boost, cuk, SEPIC, and so on. However, the derived multioutput converters suffer from the hard-switching operation and nonisolation. Li *et al.* [32] present a secondary-side modulated dc–dc topology with high-frequency isolation, which can achieve ZVS over a wide load range. The secondary-side modulated structure can be extended to provide multioutput, and the multioutput is controlled independently and isolated from each other. However, the presented converter cannot achieve ZVS over the full load range, and moreover, the secondary side is changed into an active rectifier, which will increase the control complexity and system cost.

In order to alleviate the aforementioned constraints and limitations, this article proposes a hybrid modulated multioutput dc–dc topology. The proposed converter is derived from integrating the three-phase *LLC* resonant converter and the full-bridge converter. Hybrid modulation of pulse frequency modulation (PFM) and phase shift control is used in the proposed converter. One of the contributions is that the output voltages of the proposed topology are controlled by the pulse frequency and the phase shift angles. Furthermore, the other contribution is that the three-phase *LLC* resonant converter has smaller resonant current and output current ripples, which will increase the system efficiency. Moreover, the multioutput voltages are isolated from each other by the high-frequency transformer, and the soft-switching operation is achieved without requiring an additional auxiliary circuit within the entire load range. Therefore, the proposed converter has a compact, efficient, and cost-effective topology with reduced numbers of power switches.

This article is organized as follows. The proposed topology, circuit configuration description, and operational principles analysis are exhibited in Section II. The characteristics and design considerations of the proposed multioutput converter are analyzed in Section III, which demonstrates that the multioutput is controlled independently without cross-regulation. Section VI exhibits the experimental results, which validates the feasibility and effectiveness of the proposed topology. Finally, the conclusions are made from the investigation in Section V.

## II. Proposed Hybrid Multioutput Converter and Operation Principles

### *A. Derivation of Proposed Hybrid Modulated Multioutput Converter*

The resonant converter and the full-bridge converter are two different kinds of commonly used high-frequency isolated dc–dc converters. The output voltage of the resonant converter is modulated by the switching frequency, while the output voltage of the full-bridge converter is modulated by the phase shift between the bridge branches irrelevant to the switching frequency. The three-phase *LLC* resonant dc–dc converter that is commonly used in the high power level is shown in Fig. 1; the three-phase *LLC* resonant dc–dc converter can achieve automatic current sharing by interconnecting the primary sides into a common Y-node and the secondary sides into a common Y-node, which has been proven in [29] and [30]. Fig. 1(b) shows the voltages between the midpoints of the bridge branches that are symmetric square waves and can be used as the input voltage in the full-bridge converter.

The multioutput converter is derived from the integration of the three-phase *LLC* resonant dc–dc converter and the full-bridge dc–dc converter, which is shown in Fig. 2. Fig. 2(a) presents a dual-output circuit topology that the main output voltage $V_{\text{out}}$ is derived from the three-phase *LLC* resonant dc–dc converter, bridge $A$ and $B$ form a full-bridge dc–dc converter, and the additional auxiliary output voltage $V_{\text{aux}}$ is the output voltage of the full-bridge dc–dc converter. Fig. 2(b) presents a triple-output circuit topology that the main output $V_{\text{out}}$ is derived from the three-phase *LLC* resonant dc–dc converter, bridges $A$, $B$, and $C$ form two full-bridge dc–dc converters, and two additional auxiliary output voltages $V_{\text{aux1}}$ and $V_{\text{aux2}}$ are the output voltages the two full-bridge dc–dc converters. Fig. 2(c) presents a quadruple-output circuit topology that has the main output voltage $V_{\text{out}}$ and three additional auxiliary output voltages $V_{\text{aux1}}$, $V_{\text{aux2}}$, and $V_{\text{aux3}}$. The proposed multioutput converter features attributes of lower cost and higher power density without cross-regulation by the combination of the three-phase *LLC* resonant dc–dc converter and the full-bridge dc–dc converter.

This article takes the topology of triple outputs, as shown in Fig. 2(b), as an example to analyze the proposed multioutput converter, the output voltage $V_{\text{out}}$ is regulated by the switching frequency, and the two additional auxiliary output voltages $V_{\text{aux1}}$ and $V_{\text{aux2}}$ will be left unregulated, as the phase shift angles between two bridge branches are 120°. As shown in Fig. 2(b), MOSFETs $S_1$, $S_2$, $S_3$, $S_4$, $S_5$, and $S_6$ are used to form a two-level three-phase structure. Three resonant capacitors $C_{r1}$, $C_{r2}$, and $C_{r3}$, three resonant inductors $L_{r1}$, $L_{r2}$, and $L_{r3}$, and three magnetizing inductance $L_{m1}$, $L_{m2}$, and $L_{m3}$ form a three-phase *LLC* resonant tank. Two dc blocking capacitors $C_{B1}$ and $C_{B2}$ and transformers $T_{\text{axu1}}$ and $T_{\text{aux2}}$ with leakage inductance $L_{k1}$ and $L_{k2}$ consist of two full-bridge converters.

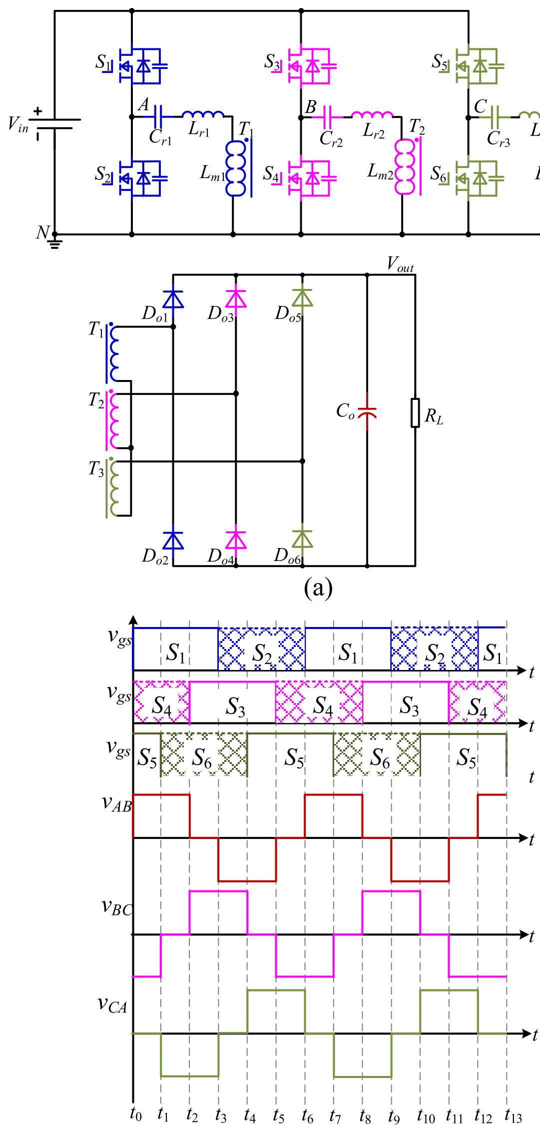

(a)

(b)

Fig. 1. Circuit diagram of three-phase *LLC* resonant dc–dc converter. (a) Three-phase *LLC* resonant dc–dc converter. (b) Voltages between the midpoints of bridge branches.

### B. Operational Principles of the Proposed Hybrid Modulated Multioutput Converter

The proposed hybrid multioutput converter is derived from integrating the three-phase *LLC* resonant converter and the full-bridge converter, and the operational principles are similar to the resonant converter and the full-bridge converter. The proposed converter is modulated by the pulse frequency with a pulsewidth of 0.5. Figs. 3 and 4, respectively, show the operational modes and the principal waveforms of the proposed converter. In Fig. 4, $v_{gs1}$, $v_{gs2}$, $v_{gs3}$, $v_{gs4}$, $v_{gs5}$, and $v_{gs6}$ are the gate-driving signals for the power switches $S_1$, $S_2$, $S_3$, $S_4$, $S_5$, and $S_6$, respectively. $i_{Lr1}$, $i_{Lr2}$, and $i_{Lr3}$ are the resonant currents, and $i_{Lk1}$ and $i_{Lk2}$ are the currents of the full-bridge converters. $i_D$ is the output current ripple of the three-phase resonant converter. The output voltage $V_{\text{out}}$ is regulated by the switching frequency, while, in order to get better current sharing performance of the three-phase *LLC* resonant converter, the phase shift angles between the two bridge branches $\varphi_1$ and $\varphi_2$ are designed to be 120°.

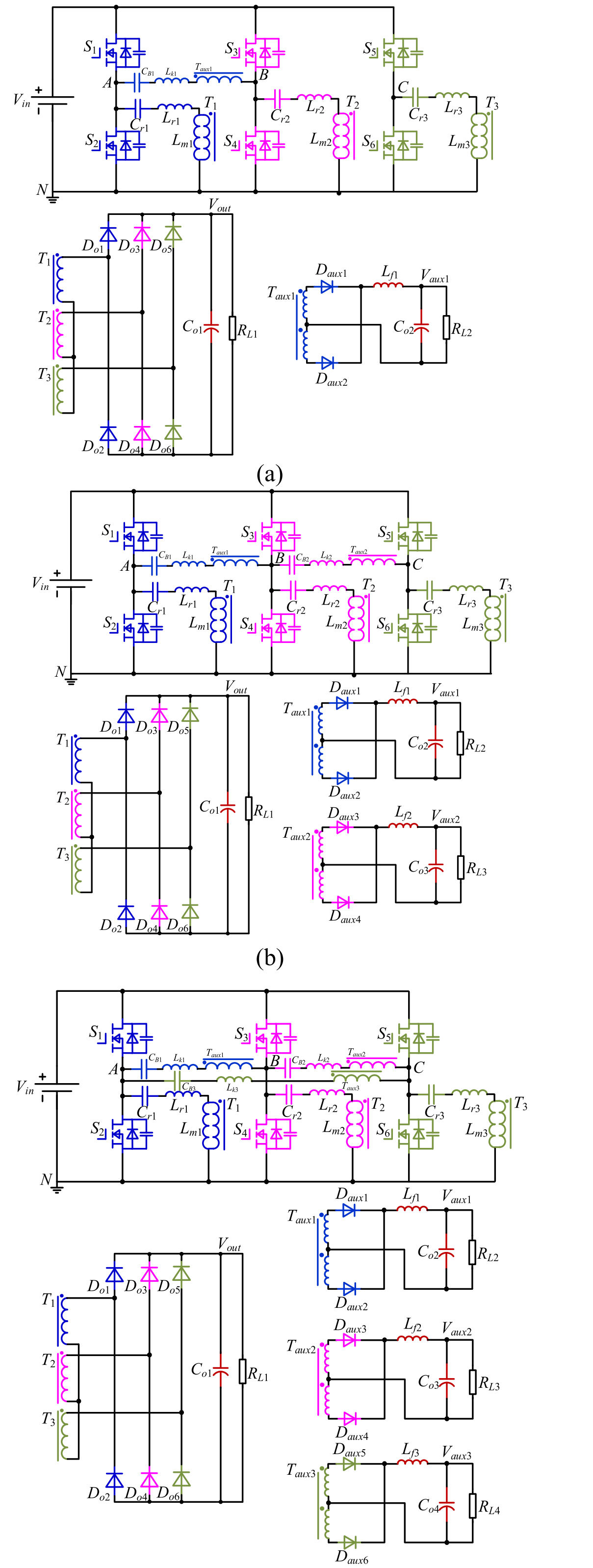

(a)

(b)

(c)

Fig. 2. Topology derivation based on modulated three-phase *LLC* resonant dc–dc converter and full-bridge converter. (a) Topology of dual outputs. (b) Topology of triple outputs. (c) Topology of quadruple outputs.

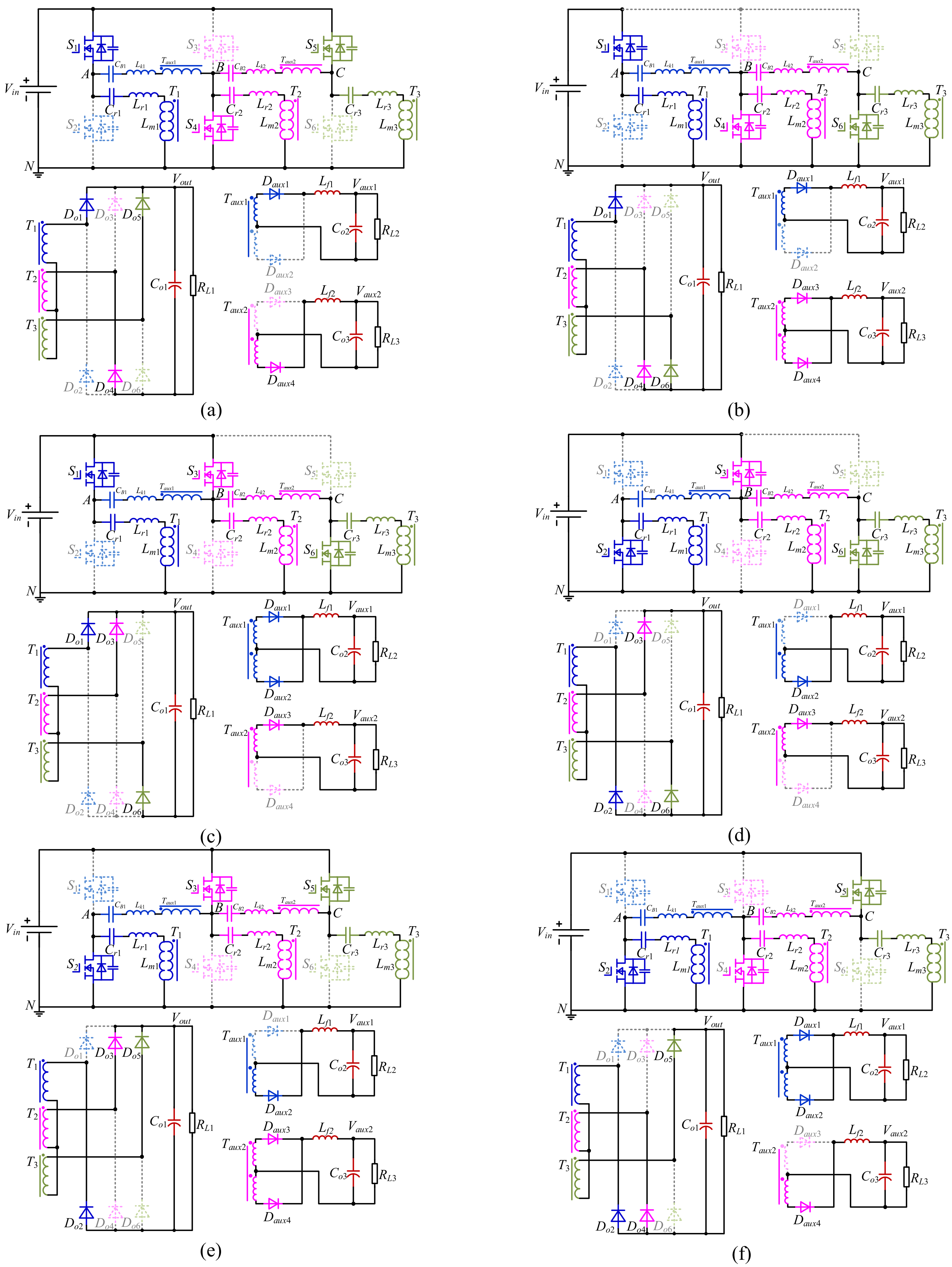

Fig. 3. Operational modes of the proposed converter. (a) Interval 1 ($t_0 \leq t < t_1$). (b) Interval 2 ($t_1 \leq t < t_2$). (c) Interval 3 ($t_2 \leq t < t_3$). (d) Interval 4 ($t_3 \leq t < t_4$). (e) Interval 5 ($t_4 \leq t < t_5$). (f) Interval 6 ($t_5 \leq t \leq t_6$).

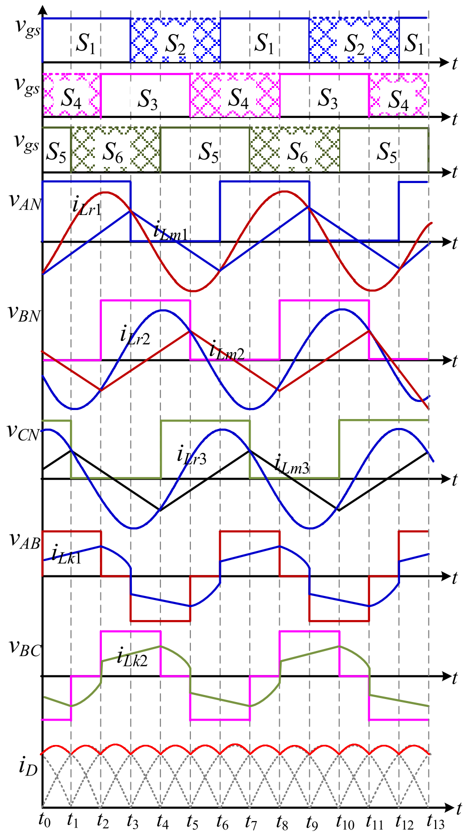

Fig. 4. Principal waveforms of the proposed converter.

For sake of simplicity, some assumptions are made, which as listed as follows.

1) The deadband intervals of MOSFETs are ignored.

2) The two full-bridge converters are designed to be operated at the continuous conduction mode.

4) The values of the three-phase resonant tank are assumed to be equal: the resonant capacitors $C_{r1}$, $C_{r2}$, and $C_{r3}$ are assumed to be the same, $C_{r1} = C_{r2} = C_{r3} = C_r$; the resonant inductors $L_{r1}$, $L_{r2}$, and $L_{r3}$ are assumed to be the same, $L_{r1} = L_{r2} = L_{r3} = L_r$; and the magnetizing inductance $L_{m1}$, $L_{m2}$, and $L_{m3}$ are assumed to be the same, $L_{m1} = L_{m2} = L_{m3} = L_m$.

5) The transformers $T_1$, $T_2$, and $T_3$ have a turn ratio of $n = n_1 = n_2 = n_3 = N_{p1}/N_{s1}$; the transformer $T_{\text{aux1}}$ has a turn ratio of $n_{\text{aux1}} = N_{p\_\text{aux1}}/N_{s\_\text{aux1}}$; and the transformer $T_{\text{aux2}}$ has a turn ratio of $n_{\text{aux2}} = N_{p\_\text{aux2}}/N_{s\_\text{aux2}}$.

6) The conducting voltage drop and equivalent resistance of output-rectified diodes are ignored.

7) The phase shifts $\varphi_1$ and $\varphi_2$ between the bridge branches are designed to be 120°.

*Interval 1 [$t_0 \le t < t_1$; see Fig. 3(a)]:* This interval starts when switch $S_1$ turns on and switch $S_2$ turns off at $t_0$. Before $t_0$, switches $S_4$ and $S_5$ have been already conducted. The resonant inductors resonate with the resonant capacitors; therefore, the resonant currents $i_{Lr1}$, $i_{Lr2}$, and $i_{Lr3}$ vary in the sinusoidal waveform by resonance. The input voltages of the resonant tanks' $A$ phase and $C$ phase are $+V_{\text{in}}$, while the input voltage of the resonant tank $B$ phase is 0. The rectifier diodes $D_{o1}$, $D_{o4}$, and $D_{o5}$ conduct during this mode. The magnetizing currents $i_{Lm1}$ and $i_{Lm3}$ increase linearly by the clamped voltage, while $i_{Lm2}$ decreases linearly. In the full-bridge converters, the voltage $v_{AB}$ between points $A$ and $B$ is $+V_{\text{in}}$, and the current $i_{Lk1}$ increases linearly. The voltage $v_{BC}$ between point $B$ and $C$ $v_{BC}$ is $-V_{\text{in}}$, and the current $i_{Lk2}$ decreases linearly. The currents of the full-bridge converter are expressed as follows:

$$\begin{cases} i_{Lk1}(t) = i_{Lk1}(t_0) + \dfrac{V_{\text{in}} - n_{\text{aux1}} V_{\text{aux1}}}{L_{k1} + n_{\text{aux1}}^2 L_{f1}}(t - t_0) \\ i_{Lk2}(t) = i_{Lk2}(t_0) + \dfrac{V_{\text{in}} - n_{\text{aux2}} V_{\text{aux2}}}{L_{k2} + n_{\text{aux2}}^2 L_{f2}}(t - t_0). \end{cases} \tag{1}$$

*Interval 2 [$t_1 \le t < t_2$; see Fig. 3(b)]:* This interval starts when switch $S_5$ turns off and switch $S_6$ turns on at $t_1$. Switches $S_1$ and $S_4$ have been already conducted before $t_1$. The resonant inductors go on resonating with the resonant capacitors, and the resonant currents $i_{Lr1}$, $i_{Lr2}$, and $i_{Lr3}$ vary in the sinusoidal waveform. The input voltage of resonant tank $A$ is $+V_{\text{in}}$, and the input voltages of resonant tanks $B$ and $C$ are $+V_{\text{in}}$. The rectifier diodes $D_{o1}$, $D_{o4}$, and $D_{o5}$ conduct during this mode. The magnetizing currents $i_{Lm1}$ and $i_{Lm3}$ increase linearly by the clamped voltage, and the magnetizing current $i_{Lm2}$ decreases linearly. In the full-bridge converters, the voltage $v_{AB}$ between points $A$ and $B$ $v_{AB}$ is $+V_{\text{in}}$, and the current $i_{Lk1}$ goes on increasing, while the voltage $v_{BC}$ between points $B$ and $C$ $v_{BC}$ is 0, and the rectifier diodes $D_{\text{aux3}}$ and $D_{\text{aux4}}$ are conducting simultaneously. The capacitor $C_{B2}$ and the inductor $L_{k2}$ begin to resonate. The currents are expressed as follows:

$$\begin{cases} i_{Lk1}(t) = i_{Lk1}(t_1) + \dfrac{V_{\text{in}} - n_{\text{aux1}} V_{\text{aux1}}}{L_{k1} + n_{\text{aux1}}^2 L_{f1}}(t - t_1) \\ i_{Lk2}(t) = \dfrac{-V_{\text{in}} - v_{CB2}(t_1)}{Z_{B2}} \sin(\omega_{B2}(t - t_1)) + i_{Lk2}(t_1) \\ \qquad \cos(\omega_{B2}(t - t_1)). \end{cases} \tag{2}$$

*Interval 3 [$t_2 \le t < t_3$; see Fig. 3(c)]:* This interval starts when switch $S_4$ turns off and switch $S_3$ turns on at $t_2$. The switches $S_1$ and $S_6$ have been already conducted before $t_2$. The resonant currents $i_{Lr1}$, $i_{Lr2}$, and $i_{Lr3}$ vary in the sinusoidal waveform by resonance. The input voltages of the resonant tank phase $A$ are $+V_{\text{in}}$, while the input voltages of the resonant tank phase $B$ and phase $C$ are 0. The rectifier diodes $D_{o2}$, $D_{o3}$, and $D_{o6}$ conduct during this mode. The magnetizing currents $i_{Lm1}$ and $i_{Lm2}$ increase linearly by the clamped voltage, while the magnetizing current $i_{Lm3}$ decreases linearly. In the full-bridge converters, the voltage $v_{AB}$ between points $A$ and $B$ is 0, and the diodes $D_{\text{aux1}}$ and $D_{\text{aux2}}$ are conducting simultaneously. The capacitor $C_{B1}$ and inductor $L_{k1}$ begin to resonate. While the voltage $v_{BC}$ between points $B$ and $C$ is $+V_{\text{in}}$, the current $i_{Lk2}$ begins to increase linearly.

The currents are expressed as follows:

$$\begin{cases} i_{Lk1}(t) = \dfrac{-V_{\text{in}} - v_{CB1}(t_2)}{Z_{B1}} \sin(\omega_{B1}(t-t_2)) + i_{Lk1}(t_2) \\ \qquad \cos(\omega_{B1}(t-t_2)) \\ i_{Lk2}(t) = i_{Lk2}(t_2) + \dfrac{V_{\text{in}} - n_{\text{aux2}} V_{\text{aux2}}}{L_{k2} + n_{\text{aux2}}^2 L_{f2}}(t-t_2). \end{cases} \tag{3}$$

*Interval 4 [$t_3 \le t < t_4$; see Fig. 3(d)]:* This interval starts when switch $S_1$ turns off and switch $S_2$ turns on at $t_3$. The switches $S_3$ and $S_6$ have been already conducted before $t_3$. The resonant currents $i_{Lr1}$, $i_{Lr2}$, and $i_{Lr3}$ vary in the sinusoidal waveform by resonance. The input voltages of resonant tank phases $A$ and $C$ are 0, while the input voltage of resonant tank phase $B$ is $+V_{\text{in}}$. The rectifier diodes $D_{o2}$, $D_{o3}$, and $D_{o6}$ conduct during this mode. The magnetizing currents $i_{Lm1}$ and $i_{Lm3}$ decrease linearly by the clamped voltage, while the magnetizing current $i_{Lm2}$ increases linearly. In the full-bridge converters, the voltage $v_{AB}$ between points $A$ and $B$ is $-V_{\text{in}}$, and the current $i_{Lk1}$ begins to decrease linearly. The voltage $v_{BC}$ between points $B$ and $C$ is $+V_{\text{in}}$, and the current $i_{Lk2}$ goes on increasing linearly. The currents are expressed as follows:

$$\begin{cases} i_{Lk1}(t) = i_{Lk1}(t_3) + \dfrac{V_{\text{in}} - n_{\text{aux1}} V_{\text{aux1}}}{L_{k1} + n_{\text{aux1}}^2 L_{f1}}(t-t_3) \\ i_{Lk2}(t) = i_{Lk2}(t_3) + \dfrac{V_{\text{in}} - n_{\text{aux2}} V_{\text{aux2}}}{L_{k2} + n_{\text{aux2}}^2 L_{f2}}(t-t_3). \end{cases} \tag{4}$$

*Interval 5 [$t_4 \le t < t_5$; see Fig. 3(e)]:* This interval starts when switch $S_6$ turns off and switch $S_5$ turns on at $t_4$. The switches $S_2$ and $S_3$ have been already conducted before $t_4$. The resonant currents $i_{Lr1}$, $i_{Lr2}$, and $i_{Lr3}$ vary in the sinusoidal waveform by resonance. The input voltage of the resonant tank phase $A$ is 0, and the input voltages of the resonant tank phase $B$ and phase $C$ are $+V_{\text{in}}$. The rectifier diodes $D_{o2}$, $D_{o3}$, and $D_{o5}$ are conducting. The magnetizing current $i_{Lm1}$ decreases linearly by the clamped voltage, while the magnetizing currents $i_{Lm2}$ and $i_{Lm3}$ increase linearly. In the full-bridge converters, the voltage $v_{AB}$ between points $A$ and $B$ $v_{AB}$ is $-V_{\text{in}}$; as a result, the current $i_{Lk1}$ decreases linearly. The voltage $v_{BC}$ between points $B$ and $C$ $v_{BC}$ is 0, and the rectifier diodes $D_{\text{aux3}}$ and $D_{\text{aux4}}$ are conducting simultaneously. The capacitor $C_{B2}$ and inductor $L_{k2}$ begin to resonate. The currents are expressed as follows:

$$\begin{cases} i_{Lk1}(t) = i_{Lk1}(t_4) + \dfrac{V_{\text{in}} - n_{\text{aux1}} V_{\text{aux1}}}{L_{k1} + n_{\text{aux1}}^2 L_{f1}}(t-t_4) \\ i_{Lk2}(t) = \dfrac{-V_{\text{in}} - v_{CB2}(t_4)}{Z_{B2}} \sin(\omega_{B2}(t-t_4)) + i_{Lk2}(t_4) \\ \qquad \cos(\omega_{B2}(t-t_4)). \end{cases} \tag{5}$$

*Interval 6 [$t_5 \le t \le t_6$; see Fig. 3(f)]:* This interval starts when switch $S_3$ turns off and $S_4$ turns on at $t_5$. The switches $S_2$ and $S_5$ have been already conducted. The resonant currents $i_{Lr1}$, $i_{Lr2}$, and $i_{Lr3}$ vary in the sinusoidal waveform by resonance. The input voltages of the resonant tank phase $A$ and phase $B$ are 0; the input voltage of the resonant tank phase $C$ is $+V_{\text{in}}$. The rectifier diodes $D_{o2}$, $D_{o4}$, and $D_{o5}$ are conducting. The magnetizing current $i_{Lm1}$ goes on decreasing linearly, while the magnetizing current $i_{Lm2}$ begins to decrease linearly, and the magnetizing current $i_{Lm3}$ goes on increasing linearly. In the full-bridge converters, the voltage $v_{AB}$ between points $A$ and $B$ $v_{AB}$ is 0, and the rectifier diodes $D_{\text{aux1}}$ and $D_{\text{aux2}}$ are conducting simultaneously. The capacitor $C_{B1}$ and inductor $L_{k1}$ begin to resonate. The voltage $v_{BC}$ between points $B$ and $C$ $v_{BC}$ is $-V_{\text{in}}$, and the current begins to decrease. The currents are expressed as follows:

$$\begin{cases} i_{Lk1}(t) = \dfrac{-V_{\text{in}} - v_{CB1}(t_5)}{Z_{B1}} \sin(\omega_{B1}(t-t_5)) + i_{Lk1}(t_5) \\ \qquad \cos(\omega_{B1}(t-t_5)) \\ i_{Lk2}(t) = i_{Lk2}(t_5) + \dfrac{V_{\text{in}} - n_{\text{aux2}} V_{\text{aux2}}}{L_{k2} + n_{\text{aux2}}^2 L_{f2}}(t-t_5). \end{cases} \tag{6}$$

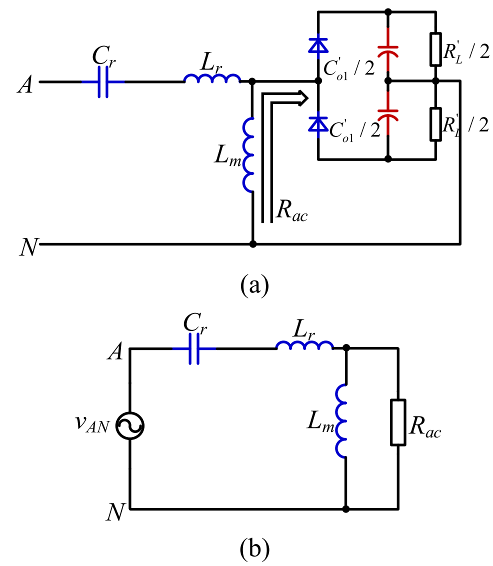


Fig. 5. Equivalent single-phase circuit by FHA. (a) Equivalent circuit of one phase. (b) Per-phase phasor equivalent circuit.

## III. Characteristics and Analysis

The proposed topology is derived from the integration of the three-phase *LLC* resonant converter and the full-bridge converters. The multioutput is regulated by the hybrid modulation of PFM and PWM without cross-regulation. This section analyzes the characteristics of the three-phase *LLC* resonant converter first and then analyzes the characteristics of the full-bridge converter. Finally, a design example is presented to illustrate the design procedure.

### *A. Characteristics Analysis of the Three-Phase Resonant Converter*

The converter is analyzed using the fundamental harmonic analysis (FHA). All the components are reflected on the primary side, and the circuit can be simplified into the one-phase circuit, as shown in Fig. 5(a); the per-phase phasor equivalent circuit can be depicted in Fig. 5(b). The input voltage in Fig. 5(b) is represented by the fundamental component of the square-wave voltage across AN; the equivalent output resistance can be derived as [33]

$$R_{\mathrm{ac}} = \frac{8n^2}{\pi^2} R_L. \tag{7}$$

Based on the FHA, the voltage gain of the per-phase *LLC* resonant circuit can be expressed as follows:

$$M_H = \frac{1}{n} \frac{1}{\sqrt{\left(1 + k - \frac{k}{f_n^2}\right)^2 + Q^2\left(f_n - \frac{1}{f_n}\right)^2}} \tag{8}$$

where $k$ is the inductance ratio, $f_n$ is the normalized frequency, and $Q$ is the quality factor, which are defined as follows:

$$k = \frac{L_r}{L_m}, \quad f_n = \frac{f_s}{f_r}, \quad Q = \frac{\sqrt{L_r/C_r}}{R_{\mathrm{ac}}} \tag{9}$$

where $f_s$ is the switching frequency and $f_r$ is the resonant frequency of resonant inductor $L_r$ and resonant capacitor $C_r$.

### *B. Characteristic Analysis of the Full-Bridge Converter*

The two auxiliary output voltages $V_{\mathrm{aux1}}$ and $V_{\mathrm{aux2}}$ are the output voltage of two full-bridge converters that share one bridge branch. In the conventional design of the full-bridge converter, the auxiliary inductor needs to be specially designed to help achieving soft-switching operation. However, the auxiliary inductor will cause the duty cycle loss, and the bigger the more serious. Therefore, there is a balance between the soft-switching operation and the duty cycle loss in the conventional full-bridge converter. What is worse, the soft-switching operation will lose under light load conditions, which will decrease the reliability and efficiency.

In the proposed multioutput converter, the power switches can keep the soft-switching operation within the entire load range by the existence of the *LLC* resonant tank in the proposed converter. As a consequence, the auxiliary inductor in the proposed converter does not need to be specially designed. As a consequence, the duty cycle loss caused by the auxiliary inductor can be ignored. In this article, the auxiliary inductors $L_{k1}$ and $L_{k2}$ are the leakage inductance of the transformers $T_{\mathrm{aux1}}$ and $T_{\mathrm{aux2}}$. The voltage gain of the full-bridge phase shift converter can be expressed as follows without considering the duty cycle loss:

$$M_L = \frac{\varphi}{\pi n_{\mathrm{aux}}} \tag{10}$$

where $n_{\mathrm{aux}}$ is the turns ratio of the transformer and the phase shift angle $\varphi$ in (10) is 120° in the three-phase *LLC* resonant converter.

From the above analysis, the PFM is adopted in the *LLC* resonant converter, and the PWM is adopted in the full-bridge converter. The multioutput voltages of the *LLC* resonant converter and the full-bridge converter are regulated by different categories of variables, which will not affect each other.

### *C. Design Considerations*

A design example is presented to illustrate the design procedure. The proposed converter is designed and built according to the following key specifications.

1) *Input voltage $V_{\mathrm{in}}$:* 400 $V_{\mathrm{DC}}$.
2) *Main Output Voltage $V_{\mathrm{out}}$:* 200 V–400 $V_{\mathrm{DC}}$.
3) *Auxiliary Output Voltage $V_{\mathrm{aux1}}$:* 36 $V_{\mathrm{DC}}$.
4) *Auxiliary Output Voltage $V_{\mathrm{aux2}}$:* 48 $V_{\mathrm{DC}}$.
5) *Maximum Output Power of Main Output Voltage $P_{\mathrm{out}}$:* 1 kW.
6) *Maximum Output Power of Auxiliary Output Powers $P_{\mathrm{aux1}}$ and $P_{\mathrm{aux2}}$:* $P_{\mathrm{aux1}} = 200$ W and $P_{\mathrm{aux2}} = 200$ W.

*1) Selection of the Resonant Tank Components:* To determine the values of the resonant tank components, it is necessary to select the turns ratio of the transformer first. The turns ratio is determined that the efficiency of the converter in the mid-voltage (300 V) is maximized since the converter is expected to work at the mid-voltage most of the time. The voltage gain of the three-phase *LLC* resonant is expressed in (10); for the prototype circuit, the turns ratio is determined by assuming that the converter operates with voltage gain $M_H = 1$ so that the turns ratio can be calculated as follows:

$$n = \frac{V_{\mathrm{in}}}{V_{\mathrm{out}}} = 1 \times \frac{400}{300} \approx 1.5. \tag{11}$$

The turns ratio $n$ is determined to be 1.5. The maximum voltage gain is $M_{H\_\max} = V_{\mathrm{out\_max}}/V_{\mathrm{in}} = 1$, and the minimum voltage gain is $M_{H\_\min} = V_{\mathrm{out\_min}}/V_{\mathrm{in}} = 0.5$.

The resonant frequency $f_r$ is determined to be 100 kHz in the prototype circuit, and the resonant circuit's parameters can be calculated at full load

$$\begin{aligned} C_r &= \frac{1}{2\pi \times Q \times f_r \times R_{\mathrm{ac}}} \\ &= \frac{1}{2\pi \times 0.45 \times 100 \times 10^3 \times 73} = 48.4 \text{ nF} \Rightarrow 47 \text{ nF} \end{aligned} \tag{12}$$

where $Q$ is the load factor, whose value is usually selected ranging from 0.3 to 0.5 when determining the circuit parameters. $R_{\mathrm{ac}}$ is equivalent load resistance that can be calculated as follows:

$$R_{\mathrm{ac}} = \frac{8 \times n^2}{\pi^2} \times \frac{V_{\mathrm{out}}}{I_{\mathrm{out}}} = \frac{8 \times 1.5^2}{\pi^2} \times \frac{200}{5} = 73\ \Omega. \tag{13}$$

The resonant capacitor $C_r$ is determined to be 47 nF. The resonant inductor $L_r$ can be determined as follows:

$$\begin{aligned} L_r &= \frac{1}{(2\pi \times f_r)^2 C_r} = \frac{1}{\left(2\pi \times 100 \times 10^3\right)^2 \times 47 \times 10^{-9}} \\ &= 53\ \mu\text{H}. \end{aligned} \tag{14}$$

The resonant inductor $L_r$ is determined to be 53 $\mu$H.

*2) Selection of Components of Full-Bridge Converter:* The power switches in the proposed converter can keep ZVS within the entire load range by the existence of the three-phase *LLC* resonant tank. The inductor in the full-bridge converter does not need to be specially designed, and the only component that needs to be determined is the turns ratio of the transformer. The voltage gain of the full-bridge converter is expressed in (10), the phase shift angle $\varphi$ is 120°, and the turns ratio of the transformer is determined as follows:

$$n_{\mathrm{aux}} = \frac{V_{\mathrm{in}}}{V_{\mathrm{aux}}} \times \frac{120}{180}. \tag{15}$$

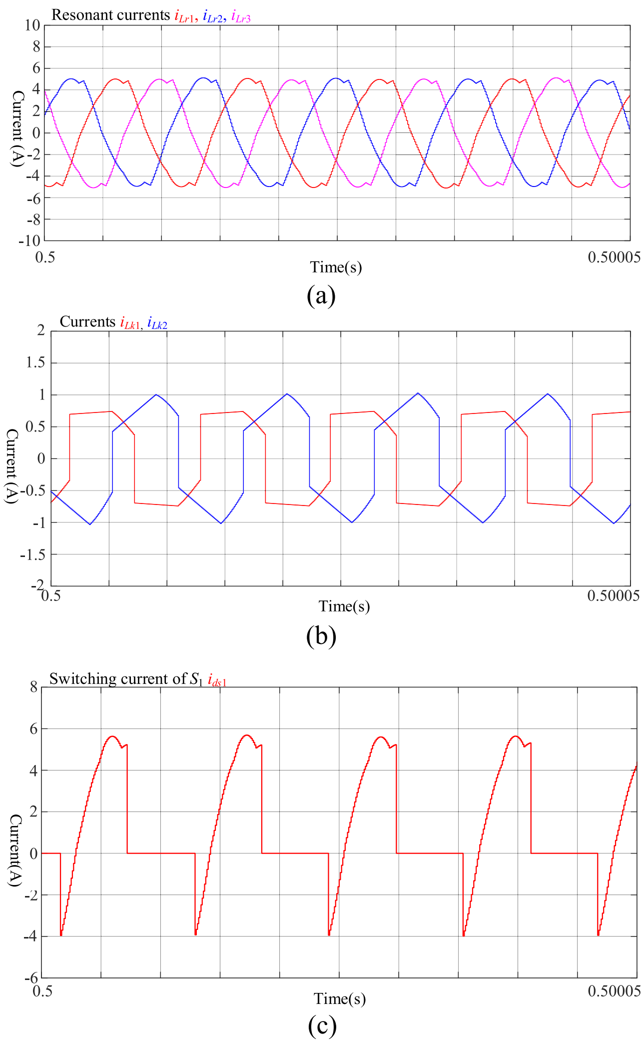


Fig. 6. Simulated waveforms of the proposed multioutput converter at $V_{\mathrm{out}} =$ 300 V, $V_{\mathrm{aux1}} = 36$ V, and $V_{\mathrm{aux2}} = 48$ V with a full load. (a) Resonant currents of the three-phase resonant tank. (b) Currents of the full-bridge converter. (c) Switching current of the power switch $S_1$.

The turns ratio $n_{\mathrm{aux1}}$ of transformer $T_{\mathrm{aux1}}$ is determined to be 7.4, and the turns ratio $n_{\mathrm{aux2}}$ of transformer $T_{\mathrm{aux2}}$ is determined to be 5.6. The key parameters used in the prototype circuit are summarized in Table I.

TABLE I
KEY CIRCUIT PARAMETERS UTILIZED IN THE EXPERIMENTAL PROTOTYPE

| Components | Parameters |
|---|---|
| Circuit parameters for the output voltage $V_{out}$ | |
| $V_{in}$ (Input voltage) | 400V |
| $V_{out}$ (Output voltage) | 200V-400V |
| $P_{out}$ (Rated output power) | 1kW |
| $f_r$ (Resonant frequency) | 100kHz |
| $L_{r1}$=$L_{r2}$=$L_{r3}$ (Resonant inductor) | 53μH |
| $C_{r1}$=$C_{r2}$=$C_{r3}$ (Resonant capacitor) | 47nF |
| $L_{m1}$=$L_{m2}$=$L_{m3}$ (Magnetizing inductor) | 120μH |
| $n_1$=$n_2$=$n_3$ (Turns ratio of transformer) | 1.5 |
| $C_{o1}$ (Output filter capacitor) | 390μF/450V |
| $S_1$-$S_6$ (Power MOSFETs) | IPW65R080CFD |
| $D_{o1}$-$D_{o6}$ (Diodes) | FDCY25S65 |
| Deadtime | 400ns |
| Circuit parameters for the output voltage $V_{aux1}$ | |
| $V_{aux1}$ (Output voltage) | 36V |
| $P_{aux1}$ (Rated output power) | 200W |
| $L_{k1}$ (Leakage inductance) | 10μH |
| $C_{B1}$ (DC blocking capacitor) | 1μF |
| $n_{\mathrm{aux1}}$ (Turns ratio of transformer) | 7.4 |
| $L_{f1}$ (Output filter inductor) | 200μH |
| $C_{o2}$ (Output filter capacitor) | 3000μF |
| $D_{aux1}$-$D_{aux2}$ (Diodes) | MBRF10H150CTG |
| Circuit parameters for the output voltage $V_{aux2}$ | |
| $V_{aux2}$ (Output voltage) | 48V |
| $P_{aux2}$ (Rated output power) | 200W |
| $L_{k2}$ (Leakage inductance) | 8μH |
| $C_{B2}$ (DC blocking capacitor) | 1μF |
| $n_{\mathrm{aux2}}$ (Turns ratio of transformer) | 5.6 |
| $L_{f2}$ (Output filter inductor) | 200μH |
| $C_{o3}$ (Output filter capacitor) | 3000μF |
| $D_{aux3}$-$D_{aux4}$ (Diodes) | MBRF10H150CTG |

## IV. SIMULATION AND EXPERIMENTAL VERIFICATIONS

### A. Simulation Results

*1) Steady-State Waveforms:* A MATLA/Simulink simulation model used to verify the analysis of the proposed multi-output topology is built and simulated. The key parameters used in the simulation model are listed in Table I. Fig. 6 shows the simulated waveforms of the proposed converter under $V_{\mathrm{out}} = 300$ V, $V_{\mathrm{aux1}} = 36$ V, and $V_{\mathrm{aux2}} = 48$ V with a full load. Fig. 6(a) shows the simulated resonant currents of the three-phase resonant tank that varies in the sinusoidal shape. Fig. 6(b) shows the primary side currents of the full-bridge converter. Fig. 6(c) shows the switching current flowing through the power switch, and it is demonstrated that zero voltage turn-on can be achieved on the power switches.

*2) Transient Waveforms:* Fig. 7 presents transient waveforms with load changes. Fig. 7(a)–(c) shows the transient waveforms with one of the output powers of switches from

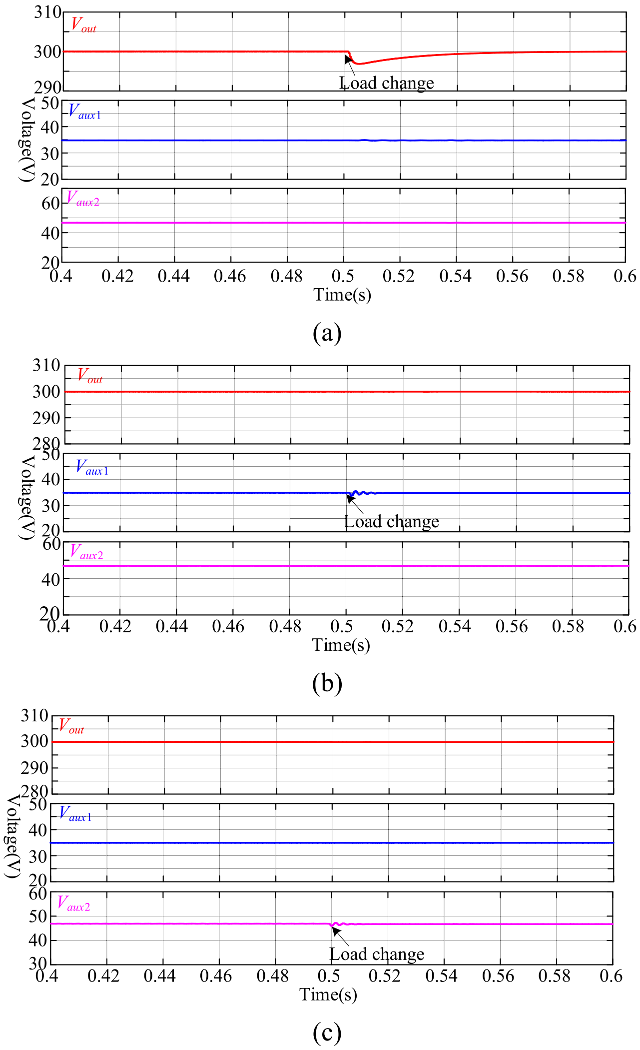


Fig. 7. Transient waveforms ($V_{\text{out}} = 300$ V, $V_{\text{aux1}} = 36$ V, and $V_{\text{aux2}} = 48$ V). (a) $P_{\text{out}}$ switches from half power to full power with $P_{\text{aux1}}$ and $P_{\text{aux2}}$ remain unchanged. (b) $P_{\text{aux1}}$ switches from half power to full power with $P_{\text{out}}$ and $P_{\text{aux2}}$ remain unchanged. (c) $P_{\text{aux2}}$ switches from half power to full power with $P_{\text{out}}$ and $P_{\text{aux1}}$ remain unchanged.

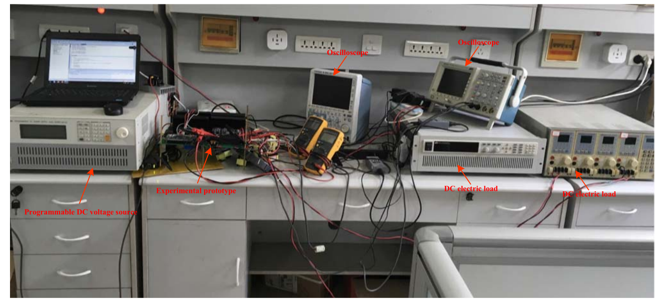

Fig. 8. Experimental platform of the proposed converter.

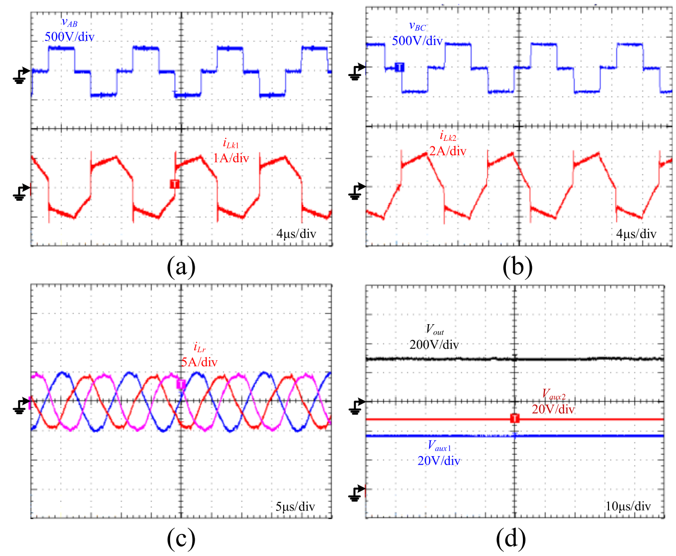


Fig. 9. Experimental waveforms at $V_{\text{out}} = 300$ V, $V_{\text{aux1}} = 36$ V, and $V_{\text{aux2}} = 48$ V with a full load. (a) Measured current waveforms of the full-bridge converter $V_{\text{aux1}}$. (b) Measured current waveforms of the full-bridge converter $V_{\text{aux2}}$. (c) Resonant currents of the three-phase resonant tank $i_{Lr1}$, $i_{Lr2}$, and $i_{Lr3}$. (d) Measured output voltages $V_{\text{out}}$, $V_{\text{aux1}}$, and $V_{\text{aux2}}$.

half power to full power, while the other two output power remains unchanged. It can be seen that the variation of one of the outputs will not affect the other two outputs.

### *B. Experimental Results and Analysis*

A 1.4-kW MOSFET-based prototype is built to verify the feasibility and effectiveness of the proposed converter, and the experimental prototype is DSP controlled with key circuit parameters listed in Table I. The inductors $L_{k1}$ and $L_{k2}$ are the leakage inductance of transformers of $T_{\text{aux1}}$ and $T_{\text{aux2}}$, respectively. The full-bridge converters are designed to be operated at continuous conduction mode, and the phase shift angles $\varphi_1$ and $\varphi_2$ between the two half-bridge branches are 120°. Fig. 8 shows the key circuit parameters utilized in the experimental prototypes. TMS320F28335 is used as the microcontroller to control the power circuit, and the parameters of the power circuits utilized in the experimental prototype are listed in Table I. The experimental platform is shown in Fig. 8, a programmable dc voltage source (from Chroma) is used as the input voltage, and two dc electric loads are used as the load for the multioutput. One dc electric load (from ITECH) is used as the load for the main output $V_{\text{out}}$; the other dc electric load (from Chroma) that has four isolated channels and two channels are used as the loads for the auxiliary outputs $V_{\text{aux1}}$ and $V_{\text{aux2}}$. Oscilloscopes are used to observe the experimental waveforms.

The maximum output power of the experimental prototype is 1.4 kW, and the output power of $V_{\text{out}}$ is 1 kW, while the output power of $V_{\text{aux1}}$ and $V_{\text{aux2}}$ is 200 W. The output voltage $V_{\text{out}}$ is modulated by the switching frequency, which is ranged from 200 to 400 V. The output voltages $V_{\text{aux1}}$ and $V_{\text{aux2}}$ are related to the phase shift angles between the three-phase interleaved bridge branches and the turns ratio of the transformers, and $V_{\text{aux1}}$ and $V_{\text{aux2}}$ are designed to be 36 and 48 V.

*1) Steady-State Waveforms:* The experimental results of the proposed multioutput converter are shown as follows. Fig. 9 shows the measured waveforms under $V_{\text{out}} = 300$ V, $V_{\text{aux1}} = 36$ V, and $V_{\text{aux2}} = 48$ V with a full load. The switching frequency of the power switches is near the resonant

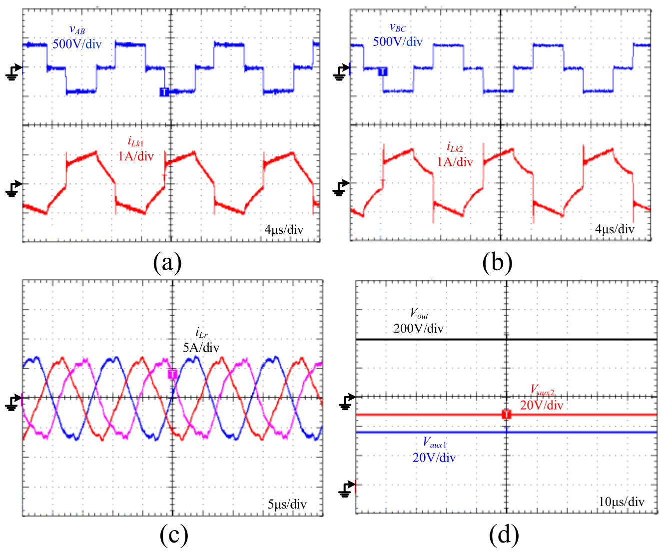


Fig. 10. Experimental waveforms at $V_{\text{out}} = 400$ V, $V_{\text{aux1}} = 36$ V, and $V_{\text{aux2}} = 48$ V with a full load. (a) Measured current waveforms of the full-bridge converter $V_{\text{aux1}}$. (b) Measured current waveforms of the full-bridge converter $V_{\text{aux2}}$. (c) Resonant currents of the three-phase resonant tank $i_{Lr1}$, $i_{Lr2}$, and $i_{Lr3}$. (d) Measured output voltages $V_{\text{out}}$, $V_{\text{aux1}}$, and $V_{\text{aux2}}$.

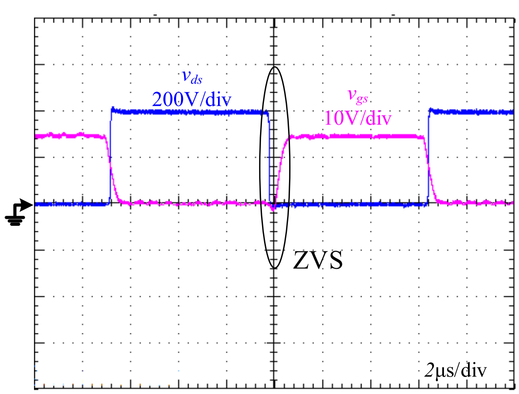


Fig. 11. Switching voltage and gate-driving signal; time scale: 2 $\mu$s/div.

frequency. The measured currents of the full-bridge converters are presented in Fig. 9(a) and (b), the resonant currents of the three-phase resonant tank are shown in Fig. 9(c), and the triple output voltages $V_{\text{out}}$, $V_{\text{aux1}}$, and $V_{\text{aux2}}$ are demonstrated in Fig. 9(d). Fig. 10 shows the measured waveforms under $V_{\text{out}} = 400$ V, $V_{\text{aux1}} = 36$ V, and $V_{\text{aux2}} = 48$ V with a full load. The switching frequency is below the resonant frequency. The measured currents of the full-bridge converters are presented in Fig. 10(a) and (b). The measured resonant currents of the three-phase resonant tank are presented in Fig. 10(c), and the triple output voltages $V_{\text{out}}$, $V_{\text{aux1}}$, and $V_{\text{aux2}}$ are demonstrated in Fig. 10(d). It can be proved from the experimental results that the resonant currents vary in the sinusoidal waveform just as in the theoretical analysis. The currents of the full-bridge converters increase/decrease linearly as the input voltage is $+V_{\text{in}}/-V_{\text{in}}$, while, during the input voltage is 0, the leakage inductance of the transformer $T_4/T_5$ begins to resonate with the dc-blocking capacitor $C_{B1}/C_{B2}$.

Fig. 11 shows the switching voltage and gate-driving signal of one of the power switches ($S_1$) under full power; it can be found that the switching voltage $V_{\text{ds}}$ falls down to zero before the gate-driving signal $V_{\text{gs}}$ turns on the power switch, which demonstrates that the ZVS operation can be ensured.

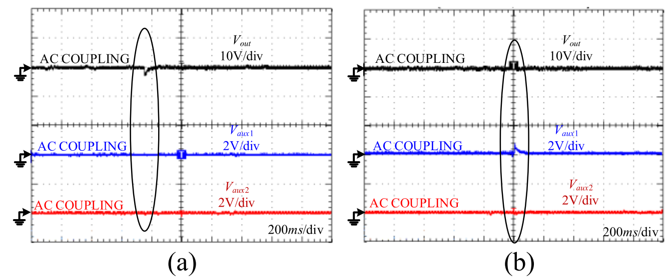


Fig. 12. Measured load transient waveforms: $P_{\text{aux1}}$ switches from half power to full power with $P_{\text{out}}$ and $P_{\text{aux2}}$ remain unchanged; time scale: 200 ms/div.

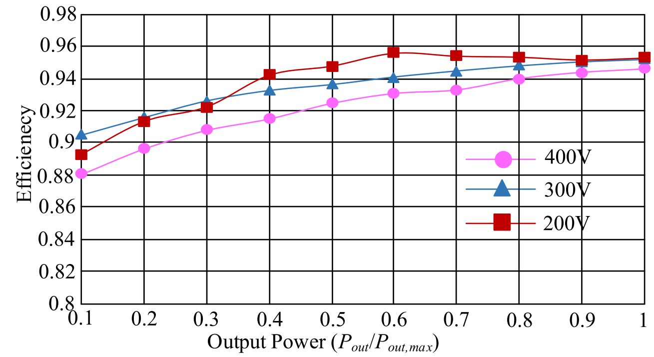


Fig. 13. Efficiency versus output power ($P_{\text{aux1}} = 200$ W and $P_{\text{aux2}} = 200$ W).

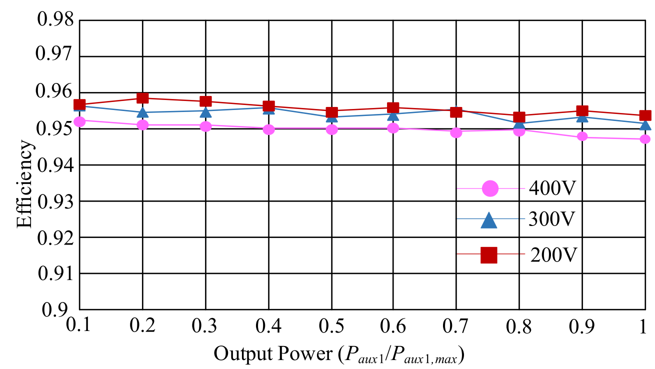


Fig. 14. Efficiency versus output power ($P_{\text{out}} = 1$ kW and $P_{\text{aux2}} = 200$ W).

*2) Transient Waveforms:* In order to prove that the proposed multioutput are free from cross-regulation, a transient experiment with load change is carried out. The load transient response waveforms are presented in Fig. 12. In order to present the variations of the output voltages during the transient response clearly, ac coupling of the output voltages is used. In Fig. 12(a), $P_{\text{aux1}}$ and $P_{\text{aux2}}$ remain at full power unchanged, while $P_{\text{out}}$ switches from half power to full power. In Fig. 12(b), $P_{\text{out}}$ and $P_{\text{aux2}}$ remain at full power unchanged, while $P_{\text{aux1}}$ switches from full power to half power. It can be found that the variation of one voltage will not affect the other two voltages. It can be demonstrated that the triple output voltages do not affect each other, and the triple outputs are free from cross-regulation.

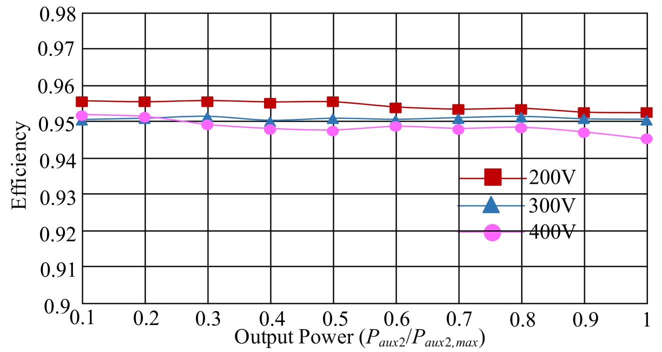


Fig. 15. Efficiency versus output power ($P_{\text{out}} = 1$ kW and $P_{au1} = 200$ W).

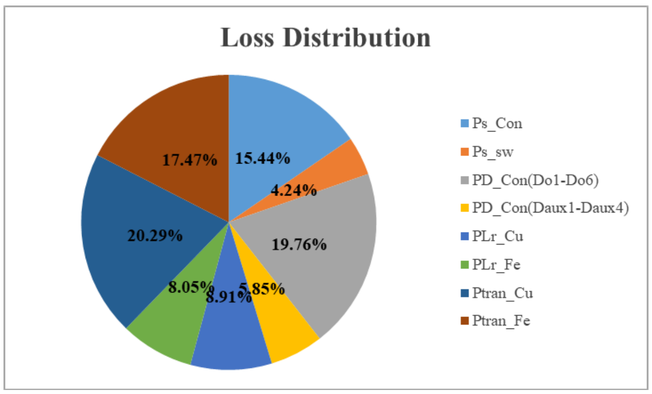


Fig. 16. Estimated loss distribution under $V_{\text{out}} = 300$ V, $V_{\text{aux1}} = 36$ V, and $V_{\text{aux2}} = 48$ V with full load (total loss = 70.74 W).

*3) Measured Efficiency:* Figs. 13–15 show the measured efficiency curve. In Fig. 13, $P_{\text{aux1}}$ and $P_{\text{aux2}}$ keep at full power unchanged, while the efficiency of the experimental prototype is measured as $P_{\text{out}}$ varies from 10% power to full power under different output voltages. The measured minimum efficiency of the prototype is 88.1% at 400-V 10% power, and the measured maximum efficiency is 95.6% at 200-V 70% power. In Fig. 14, $P_{\text{out}}$ and $P_{\text{aux2}}$ keep at full power unchanged, while the efficiency is measured as $P_{\text{aux1}}$ varies from 10% power to full power under different $V_{\text{out}}$'s. In Fig. 15, $P_{\text{out}}$ and $P_{\text{aux1}}$ keep at full power unchanged, while the efficiency is measured as $P_{\text{aux2}}$ varies from 10% load to full power under different $V_{\text{out}}$. As shown in Figs. 14 and 15, it is depicted that the efficiencies change a little, while the power of $P_{\text{out}}$ keeps unchanged. This is mainly because most of the power losses come from the three-phase resonant converter.

### C. Power Loss Analysis

A breakdown of the power loss incurred at 1.4 kW with $V_{\text{out}} = 300$ V, $V_{\text{aux1}} = 36$ V, and $V_{\text{aux2}} = 48$ V is shown in Fig. 16. The power loss calculation is based on a combination of experimental results (such as rms currents of the resonant current) and theoretical data from the datasheet (such as $R_{\text{ds(ON)}}$ of the MOSFETs and forward voltage drop $V_F$ of the diodes), and the calculation method is based on the loss calculation method in [34] and [35]. The power loss includes the switching and conduction loss of the MOSFETs, the conduction loss of diodes, the loss of inductors, and the loss of transformers. In Fig. 16, the subscripts "sw" and "con" represent the switching loss and the conduction loss, respectively. The MOSFETs can achieve ZVS, so there is only a turn-off loss. The diodes can achieve ZCS, so there is no switching loss of diodes. The subscripts "Cu" and "Fe" represent the winding loss and core loss of the magnetic components. Since the series resistance of the output capacitor is very small, the power loss of the output capacitor is ignored. From the results, it can be found that almost 54.7% of the total loss can be attributed to magnetic loss by transformers and inductors. 4.24% is switching loss as the soft-switching operation can be achieved on the power switches. By further investigating the power loss chart, the efficiency can be improved by increasing the switching frequency. By increasing the switching frequency, fewer winding turns and lower core loss are expected. Therefore, the efficiency of the converter can be improved furtherly.

## V. Conclusion

The proposed multioutput dc–dc topology is derived from the hybrid modulated three-phase *LLC* resonant converter and the full-bridge converter. With the hybrid modulation of PWM and PFM, the multioutput of the proposed converter is controlled and free from cross-regulation. In addition, the multioutput is isolated from each other by the high-frequency transformer. The power level of the auxiliary output voltages could be high. In the designed prototype circuit, the output power of the auxiliary output voltages is about two-thirds of the per-phase resonant tank of the main output voltage, while the power switches still can keep zero voltage turned on. The three-phase *LLC* resonant tank can reduce the resonant current and, thus, increase the system efficiency. Moreover, the power switches on the primary side can keep ZVS within the full load range. The proposed topology shows features of the reduced number of power switches and higher power density. In consequence, all the advantages of the proposed converter will lead to a compact, efficient, and cost-effective design. Finally, experimental results have validated the feasibility and effectiveness of the proposed converter.

## References

[1] M. Yilmaz and P. T. Krein, "Review of battery charger topologies, charging power levels, and infrastructure for plug-in electric and hybrid vehicles," *IEEE Trans. Power Electron.*, vol. 28, no. 5, pp. 2151–2169, May 2013.

[2] G. Chen, Y. Deng, J. Dong, Y. Hu, L. Jiang, and X. He, "Integrated multiple-output synchronous buck converter for electric vehicle power supply," *IEEE Trans. Veh. Technol.*, vol. 66, no. 7, pp. 5752–5761, Jul. 2017.

[3] X. Gao, H. Wu, and Y. Xing, "A multioutput LLC resonant converter with semi-active rectifiers," *IEEE J. Emerg. Sel. Topics Power Electron.*, vol. 5, no. 4, pp. 1819–1827, Dec. 2017.

[4] G. Chen, Z. Jin, Y. Liu, Y. Hu, J. Zhang, and X. Qing, "Programmable topology derivation and analysis of integrated three-port DC–DC converters with reduced switches for low-cost applications," *IEEE Trans. Ind. Electron.*, vol. 66, no. 9, pp. 6649–6660, Sep. 2019.

[5] G. Lu and P. Zhang, "A novel leakage-current-based online insulation monitoring strategy for converter transformers using common-mode and differential-mode harmonics in VSC system," *IEEE Trans. Ind. Electron.*, vol. 68, no. 2, pp. 1636–1645, Feb. 2021.

[6] G. Yang, F. Xiao, X. Fan, R. Wang, and J. Liu, "Three-phase three-level phase-shifted PWM DC–DC converter for electric ship MVDC application," *IEEE J. Emerg. Sel. Topics Power Electron.*, vol. 5, no. 1, pp. 162–170, Mar. 2017.

[7] N. Shafiei and M. Ordonez, "Improving the regulation range of EV battery chargers with L3C2 resonant converters," *IEEE Trans. Power Electron.*, vol. 30, no. 6, pp. 3166–3184, Jun. 2015.

[8] F. C. Lee, Q. Li, and A. Nabih, "High frequency resonant converters: An overview on the magnetic design and control methods," *IEEE J. Emerg. Sel. Topics Power Electron.*, vol. 9, no. 1, pp. 11–23, Feb. 2021.

[9] L. Zhao, H. Li, X. Wu, and J. Zhang, "An improved phase-shifted full-bridge converter with wide-range ZVS and reduced filter requirement," *IEEE Trans. Ind. Electron.*, vol. 65, no. 3, pp. 2167–2176, Mar. 2018.

[10] G. D. Capua, S. A. Shirsavar, M. A. Hallworth, and N. Femia, "An enhanced model for small-signal analysis of the phase-shifted full-bridge converter," *IEEE Trans. Power Electron.*, vol. 30, no. 3, pp. 1567–1576, Mar. 2015.

[11] L. Zhao, H. Li, Y. Hou, and Y. Yu, "Operation analysis of a phase-shifted full-bridge converter during the dead-time interval," *IET Power Electron.*, vol. 9, no. 9, pp. 1777–1783, Jul. 2016.

[12] J. Zhu, Q. Qian, S. Lu, W. Sun, and H. Tian, "A phase-shift triple full-bridge converter with three shared leading-legs," *IEEE J. Emerg. Sel. Topics Power Electron.*, vol. 6, no. 4, pp. 1912–1920, Dec. 2018.

[13] I.-O. Lee, "Hybrid PWM-resonant converter for electric vehicle on-board battery chargers," *IEEE Trans. Power Electron.*, vol. 31, no. 5, pp. 3639–3649, May 2016.

[14] B. Gu, J. Lai, N. Kees, and C. Zheng, "Hybrid-switching full-bridge DC–DC converter with minimal voltage stress of bridge rectifier, reduced circulating losses, and filter requirement for electric vehicle battery chargers," *IEEE Trans. Power Electron.*, vol. 28, no. 3, pp. 1132–1144, Mar. 2013.

[15] J. Liu, J. Zhang, T. Q. Zheng, and J. Yang, "A modified gain model and the corresponding design method for an LLC resonant converter," *IEEE Trans. Power Electron.*, vol. 32, no. 9, pp. 6716–6727, Sep. 2017.

[16] H.-N. Vu and W. Choi, "A novel dual full-bridge LLC resonant converter for CC and CV charges of batteries for electric vehicles," *IEEE Trans. Ind. Electron.*, vol. 65, no. 3, pp. 2212–2225, Mar. 2018.

[17] F. Musavi, M. Cracium, D. S. Gautam, and W. Eberle, "Control strategies for wide output voltage range LLC resonant DC-DC converters in battery chargers," *IEEE Trans. Veh. Technol.*, vol. 63, no. 3, pp. 1117–1125, Mar. 2014.

[18] J. Deng, C. C. Mi, R. Ma, and S. Li, "Design of LLC resonant converters based on operation-mode analysis for level two PHEV battery chargers," *IEEE/ASME Trans. Mechatronics*, vol. 20, no. 4, pp. 1595–1606, Aug. 2015.

[19] H. Wang, S. Dusmez, and A. Khaligh, "Design and analysis of a full-bridge LLC-based PEV charger optimized for wide battery voltage range," *IEEE Trans. Veh. Technol.*, vol. 63, no. 4, pp. 1603–1613, Apr. 2014.

[20] Z. Hu, Y. Qiu, L. Wang, and Y.-F. Liu, "An interleaved LLC resonant converter operating at constant switching frequency," *IEEE Trans. Power Electron.*, vol. 29, no. 6, pp. 2931–2943, Jun. 2014.

[21] K. Murata and F. Kurokawa, "An interleaved PFM LLC resonant converter with phase-shift compensation," *IEEE Trans. Power Electron.*, vol. 31, no. 3, pp. 2264–2272, Mar. 2016.

[22] Z. Hu, Y. Qiu, Y. F. Liu, and P. C. Sen, "A control strategy and design method for interleaved LLC converters operating at variable switching frequency," *IEEE Trans. Power Electron.*, vol. 29, no. 8, pp. 4426–4437, Aug. 2014.

[23] D. Moon, J. Park, and S. Choi, "New interleaved current-fed resonant converter with significantly reduced high current side output filter for EV and HEV applications," *IEEE Trans. Power Electron.*, vol. 30, no. 8, pp. 4264–4271, Aug. 2015.

[24] S. Kim, J. W. Baek, M. H. Ryu, J. H. Kim, and J. H. Jung, "The high-efficiency isolated AC–DC converter using the three-phase interleaved LLC resonant converter employing the Y-connected rectifier," *IEEE Trans. Power Electron.*, vol. 29, no. 8, pp. 4017–4028, Aug. 2014.

[25] H. Wang, Y. Chen, Y.-F. Liu, J. Afsharian, and Z. Yang, "A passive current sharing method with common inductor multiphase LLC resonant converter," *IEEE Trans. Power Electron.*, vol. 32, no. 9, pp. 6994–7010, Sep. 2017.

[26] M. Kobayashi and M. Yamamoto, "Current balance performance evaluations for transformer-linked three phase DC-DC LLC resonant converter," in *Proc. Int. Conf. Renew. Energy Res. Appl. (ICRERA)*, Nov. 2012, pp. 1–3.

[27] Y. Nakakohara, H. Otake, T. M. Evans, T. Yoshida, M. Tsuruya, and K. Nakahara, "Three phase LLC series resonant DC/DC converter using SiC MOSFETs to realize high voltage and high frequency operation," *IEEE Trans. Ind. Electron.*, vol. 63, no. 4, pp. 2103–2110, Apr. 2016.

[28] S.-H. Ahn, S.-R. Jang, and H.-J. Ryoo, "High-efficiency bidirectional three-phase LCC resonant converter with a wide load range," *IEEE Trans. Power Electron.*, vol. 34, no. 1, pp. 97–105, Jan. 2019.

[29] C. Fei, R. Gadelrab, Q. Li, and F. C. Lee, "High-frequency three-phase interleaved LLC resonant converter with GaN devices and integrated planar magnetics," *IEEE J. Emerg. Sel. Topics Power Electron.*, vol. 7, no. 2, pp. 653–663, Jun. 2019.

[30] E. Orietti, P. Mattavelli, G. Spiazzi, C. Adragna, and G. Gattavari, "Current sharing in three-phase LLC interleaved resonant converter," in *Proc. IEEE Energy Convers. Congr. Expo.*, Sep. 2009, pp. 1–8.

[31] M. B. F. Prieto, S. P. Litran, E. D. Aranda, and J. M. E. Gomez, "New single-input, multiple-output converter topologies: Combining single-switch nonisolated DC–DC converters for single-input, multiple-output applications," *IEEE Ind. Electron. Mag.*, vol. 10, no. 2, pp. 6–20, Jun. 2016.

[32] Z. Li, S. Dusmez, and H. Wang, "A novel soft-switching secondary-side modulated multioutput DC–DC converter with extended ZVS range," *IEEE Trans. Power Electron.*, vol. 34, no. 1, pp. 106–116, Jan. 2019.

[33] M. S. Almardy and A. K. S. Bhat, "Three-phase (LC)(L)-type series-resonant converter with capacitive output filter," *IEEE Trans. Power Electron.*, vol. 26, no. 4, pp. 1172–1183, Apr. 2011.

[34] C. Li and D. Xu, "Family of enhanced ZCS single-stage single-phase isolated AC–DC converter for high-power high-voltage DC supply," *IEEE Trans. Ind. Electron.*, vol. 64, no. 5, pp. 3629–3639, May 2017.

[35] C. Li, Y. Zhang, Z. Cao, and D. Xu, "Single-phase single-stage isolated ZCS current-fed full-bridge converter for high-power AC/DC applications," *IEEE Trans. Power Electron.*, vol. 32, no. 9, pp. 6800–6812, Sep. 2017.

**Guangdi Li** (Member, IEEE) received the B.E.E. degree from the College of Information Science and Engineering, Northeastern University, Shenyang, China, in 2013, and the Ph.D. degree in power electronics and electric drives from the College of Electrical Engineering, Zhejiang University, Hangzhou, China, in 2020.

He is currently a Post-Doctoral Researcher with the College of Information Science and Engineering, Northeastern University. He has published more than ten SCI- or EI-indexed papers. His current research interests include resonant dc–dc converters, and control and modeling of grid-connected converters.

Dr. Li is also a member of the IEEE PES Intelligent Grid & Emerging Technologies Satellite Committee—China. He is also an active reviewer of some peer-reviewed journals and international conferences.

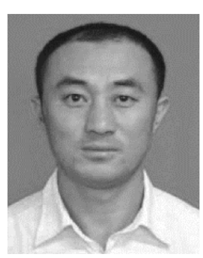

**Dongsheng Yang** (Senior Member, IEEE) received the B.S. degree in testing technology and instrumentation, the M.S. degree in power electronics and electric drives, and the Ph.D. degree in control theory and control engineering from Northeastern University, Shenyang, China, in 1999, 2004, and 2007, respectively.

He is currently a Professor with Northeastern University. He was supported by the Program for New Century Excellent Talents in University. He has authored or coauthored around 70 papers published in academic journals and conference proceedings, and three monographs. He has coinvented 80 patents. His current research interests include distributed generation, multienergy power systems, and artificial intelligence-based fault diagnosis and protection.

Prof. Yang was a recipient of the Second Prize of National Science and Technology Progress.

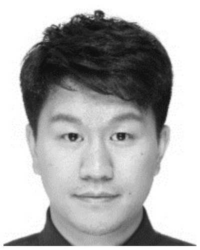

**Bowen Zhou** (Member, IEEE) received the B.Sc. and M.Sc. degrees from Wuhan University, Wuhan, China, in 2010 and 2012, respectively, and the Ph.D. degree from Queen's University Belfast, Belfast, U.K., in 2016, all in electrical engineering.

He joined the Institute of Electric Automation, College of Information Science and Engineering, Northeastern University, Shenyang, China, in 2016, where he is currently an Associate Professor. He is also a PI or a Co-I of more than ten government- or industry-sponsored projects. He has published more than 60 SCI- or EI-indexed papers. His research interests include power system operation, stability and control, vehicle to grid, energy storage and virtual energy storage, demand response, renewable energy, and energy Internet.

Dr. Zhou is also a member of IET, IAENG, CSEE, CAA, and CCF. He has served as the session chair and a TC/PC member of more than ten international conferences. He is also the Standing Director or the Director of several IEEE PES China Committees and Subcommittees.

**Yan-Fei Liu** (Fellow, IEEE) received the bachelor's and master's degrees from Zhejiang University, Hangzhou, China, in 1984 and 1987, respectively, and the Ph.D. degree from Queen's University, Kingston, ON, Canada, in 1994.

He was a Technical Advisor with the Advanced Power System Division, Nortel Networks, Ottawa, ON, Canada, from 1994 to 1999. Since 1999, he has been with Queen's University, where he is currently a Professor with the Department of Electrical and Computer Engineering. He has authored around 250 technical papers in the IEEE TRANSACTIONS and conferences. He holds 35 U.S. patents. He has written a book on "High Frequency MOSFET Gate Drivers: Technologies and Applications" published by IET. He is also a principal contributor to two IEEE standards. His current research interests include optimal application of GaN and SiC devices to achieve small-size and high-efficiency power conversion, 99% efficiency power conversion with extremely high power density, digital control technologies for high efficiency, fast dynamic response dc–dc switching converters and ac–dc converters with power factor correction, resonant converters and server power supplies, and LED drivers.

Dr. Liu received the Modeling and Control Achievement Award from the IEEE Power Electronics Society in 2017, the Premier's Research Excellence Award in 2000 in Ontario, Canada, and the Award of Excellence in Technology in Nortel in 1997. He is also the General Chair of ECCE 2019 to be held in Baltimore, USA, in 2019. He is also the Vice-President of Technical Operations of the IEEE Power Electronics Society (PELS, from 2017 to 2020). His major service to IEEE is listed as follows: a Guest Editor-in-Chief of the special issue of Power Supply on Chip of IEEE TRANSACTIONS ON POWER ELECTRONICS from 2011 to 2013, a Guest Editor for special issues of JESTPE: Miniaturization of Power Electronics Systems in 2014 and Green Power Supplies in 2016, the Co-General Chair of ECCE 2015 held in Montreal, Canada, in September 2015, and the Chair of the PELS Technical Committee (TC1) on Control and Modeling Core Technologies from 2013 to 2016 and the PELS Technical Committee (TC2) on Power Conversion Systems and Components from 2009 to 2012.

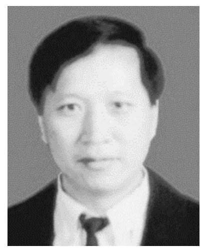

**Huaguang Zhang** (Fellow, IEEE) received the B.S. and M.S. degrees in control engineering from the Northeast Dianli University, Jilin, China, in 1982 and 1985, respectively, and the Ph.D. degree in thermal power engineering and automation from Southeast University, Nanjing, China, in 1991.

He joined the Department of Automatic Control, Northeastern University, Shenyang, China, in 1992, as a Post-Doctoral Fellow for two years. Since 1994, he has been a Professor and the Head of the School of Information Science and Engineering, Institute of Electric Automation, Northeastern University. He has authored or coauthored over 280 journal articles and conference papers, and six monographs. He has coinvented 90 patents. His main research interests are fuzzy control, stochastic system control, neural-network-based control, nonlinear control, and their applications.

Dr. Zhang was awarded the Outstanding Youth Science Foundation Award from the National Natural Science Foundation Committee of China in 2003. He was named the Cheung Kong Scholar by the Education Ministry of China in 2005. He was a recipient of the IEEE Transactions on Neural Networks 2012 Outstanding Paper Award and the Andrew P. Sage Best Transactions Paper Award 2015. He is also the E-letter Chair of the IEEE CIS Society and the Former Chair of the Adaptive Dynamic Programming & Reinforcement Learning Technical Committee on the IEEE Computational Intelligence Society.